npj | quantum materials

Article

Published in partnership with Nanjing University

https://doi.org/10.1038/s41535-025-00734-x

Giant tunability of superlattice excitations in chiral $Cr_{1/3}TaS_2$

J. L. Musfeldt[1,2] ✉, Y. Gu[1], J. T. Haraldsen[3], K. Du[4,5], P. Yapa[6], J. Yang[6], D. G. Mandrus[7,8], S. -W. Cheong[4,5] & Z. Liu[9]

Layered chalcogenides are superb platforms for exploring tunable functionality and the impact of external stimuli, and when intercalated with metal atoms, there are opportunities to reveal unique guest–host interactions. One barrier to greater control of the collective metal monolayer excitations in these materials is the absence of detailed information about how they evolve under compression. In order to explore superlattice excitations in a series of intercalated chalcogenides, we measured the Raman scattering response of $Cr_{1/3}TaS_2$ under pressure and compared our findings with the behavior of $Cr_{1/3}NbS_2$, $Fe_{1/3}TaS_2$, and $Fe_{1/4}TaS_2$. Overall, we find that the metal monolayer excitations are sharp and strong, spanning a significant portion of the teraHertz range. Analysis reveals that chalcogen layer thickness and size of the van der Waals gap to that of the *A* site ion are sufficient to divide these materials into two classes: the Cr analogs with relatively little distortion of the metal monolayer excitations under compression and the Fe analogs that host substantial symmetry breaking. In addition to unraveling these structure-property relations, we combine pressure and strain to demonstrate that the superlattice excitation in $Cr_{1/3}TaS_2$ can be tuned in a nearly linear fashion by approximately 16% overall in frequency space—a significant advance for spintronics and photonics applications.

Intercalation is an important strategy for enhancing the functionality of van der Waals solids[1–6]. This is because layered materials such as transition metal dichalcogenides can be endowed with intriguing new properties by filling the van der Waals gap with various ions or molecules, which, in addition to their unique chemistry, break symmetry in new ways. Prominent examples include Cu_xTiSe_2 ($x = 0$–0.07) which reveals the competition between the density wave state and superconductivity as well as the development of the full superconducting dome[7–11], $Cr_{1/3}NbS_2$ and $Mn_{1/3}NbS_2$ which host chiral soliton lattices[12–22], $Co_{1/3}TaS_2$ which displays skymions in the absence of magnetic field[23,24], and even intercalated chalcogenide nanotubes[25–27]. One under-explored aspect of these materials is the properties of the intercalent itself—the extended layer of atoms, ions, or molecules that resides in the two-dimensional potential. In simple systems like Fe_xTaS_2 and Cr_xNbS_2, the atomically-thin network of metal atoms forms different patterns within the van der Waals gap depending upon the intercalant concentration ($x = 1/4, 1/3$)[28–32]. When incorporated in this manner, the metal monolayers support high-temperature magnetic ordering[6,18–20,28,33–36], tunable topological spin textures that interlock with the structure[36], complex magnetic field—temperature phase diagrams[33,34], unconventional metallicity distinct from that of the parent compound[35,37–40], and superconductivity[28,41]. The $x = 1/3$ superlattice pattern is especially interesting because it renders the materials noncentrosymmetric and chiral[29]. Off-stoichiometric analogs are attracting attention for various charge ordering patterns as well[42,43].

Intercalated chalcogenides host a wide variety of phononic excitations, some of which are quite different than those in standard van der Waals materials. In systems like $Fe_{1/4}TaS_2$, $Fe_{1/3}TaS_2$, and $Cr_{1/3}NbS_2$, the fundamental excitations of the intercalated metal monolayer can be considered as in-and out-of-plane superlattice vibrations that are highly collective in nature [Fig. 1][44,45], although this simplification neglects twisting interaction with sulfur across the van der Waals gap. Here, it's important to realize that these materials are metallic[35,39,40], so infrared-active (odd-symmetry) phonons are screened by the Drude response[37–39]. This is why we explore these features via

[1]Department of Chemistry, University of Tennessee, Knoxville, TN, 37996, USA. [2]Department of Physics and Astronomy, University of Tennessee, Knoxville, TN, 37996, USA. [3]Department of Physics, University of North Florida, Jacksonville, FL, 32224, USA. [4]Department of Physics and Astronomy, Rutgers University, Piscataway, NJ, 08854, USA. [5]Keck Center for Quantum Magnetism, Rutgers University, Piscataway, NJ, 08854, USA. [6]Department of Physics, New Jersey Institute of Technology, Newark, NJ, 07102, USA. [7]Department of Materials Science and Engineering, University of Tennessee, Knoxville, TN, 37996, USA. [8]Materials Science and Technology Division, Oak Ridge National Laboratory, Oak Ridge, TN, 37831, USA. [9]Department of Physics, University of Illinois Chicago, Chicago, IL, 60607-7059, USA. ✉e-mail: musfeldt@utk.edu

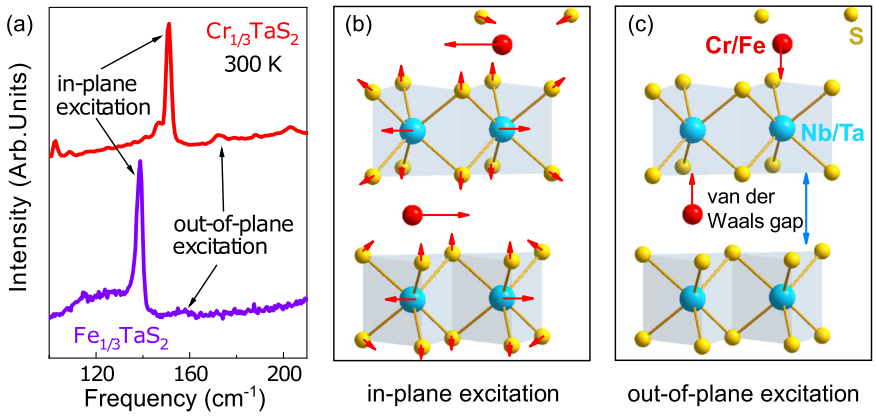

Fig. 1 | Excitations of the intercalated metal monolayer. a Close-up view of the superlattice excitations in $Cr_{1/3}TaS_2$ and $Fe_{1/3}TaS_2$. **b**, **c** Displacement patterns of the in- and out-of-plane metal monolayer excitations obtained from first-principles calculations[44].

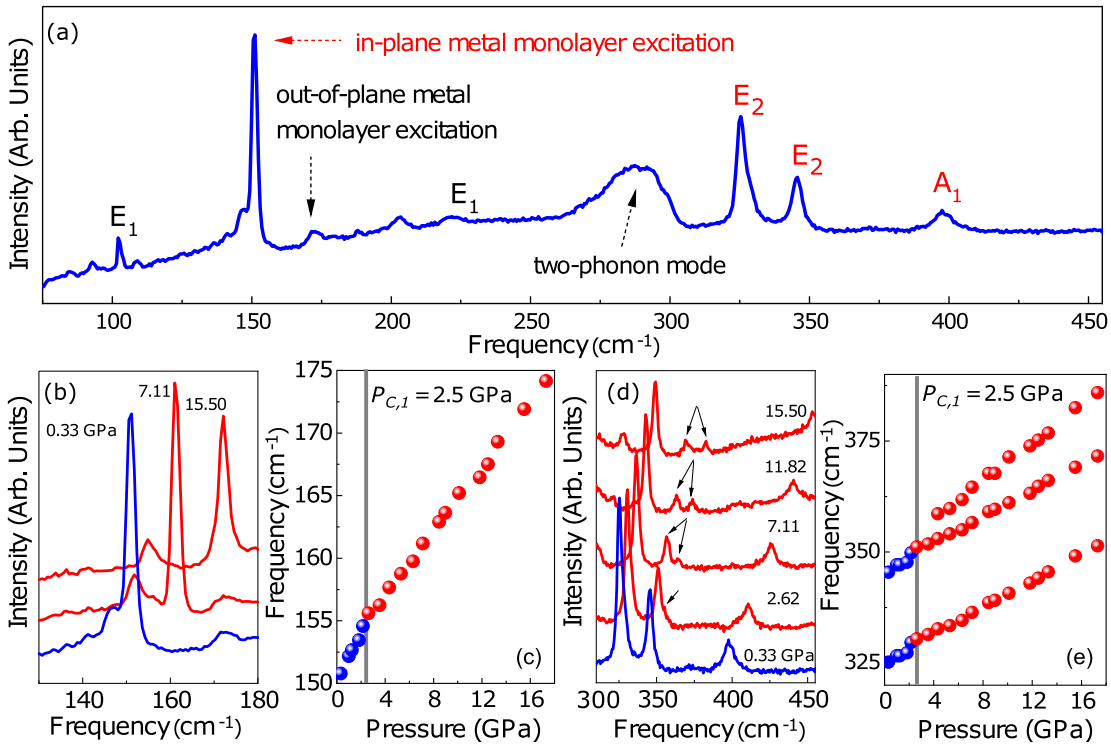

Fig. 2 | Raman scattering of $Cr_{1/3}TaS_2$ under pressure. a Raman scattering response of $Cr_{1/3}TaS_2$ at ambient conditions along with the mode assignments. **b**, **c** Close-up view of the metal monolayer excitation under pressure + frequency vs. pressure trends for this feature. The color is indicative of the phase. **d**, **e** Close-up view of higher frequency chalcogen-related modes + frequency vs. pressure trends.

Raman scattering spectroscopy[46]. The metal monolayer excitations develop with increasing intercalent concentration[45], and when fully formed, they are much stronger and sharper than the fundamental excitations of the chalcogenide lattice[44]. The in- and out-of-plane features can be distinguished by their resonance frequencies[44] and also by their polarizations[45]. Analysis reveals frequency, lifetime, and intensity trends as well as spin-phonon coupling in terms of the in-plane metal-metal distance, the size of the van der Waals gap, and the mass ratio between the intercalant and the chalcogenide layer[44]. The extent to which these metal monolayer excitations can be tuned under pressure, strain, or chemical substitution is highly under-explored.

In order to investigate the properties of intercalated chalcogenides under external stimuli, we measured the Raman scattering response of $Cr_{1/3}TaS_2$ under compression and compared our findings to the behavior of $Cr_{1/3}NbS_2$, $Fe_{1/3}TaS_2$, and $Fe_{1/4}TaS_2$. The Cr-intercalated materials are significantly more rigid than the Fe-analogs, and the relative lack of pressure-induced symmetry breaking allows the metal monolayer excitations to shift in a nearly linear fashion across important portions of the teraHertz regime. As a specific example, pressure hardens the 150 cm^{-1} in-plane metal monolayer excitation in $Cr_{1/3}TaS_2$ by about 15% whereas strain softens the same excitation by about 1%. Total tunability is on the order of 16%. A relatively narrow van der Waals gap supports this behavior. This work opens the door to pressure and strain control of spintronics devices[47–53], tunable THz resonators for LiDAR applications[44], and a greater understanding of structure–property trends[2,6] in this family of intercalated chalcogenides.

Results and discussion

$Cr_{1/3}TaS_2$ under pressure

Figure 2 summarizes the Raman scattering response of $Cr_{1/3}TaS_2$ under compression at 300 K. The intercalated metal monolayer excitations and the symmetries of the intra-layer phonons are labeled[44]. Our focus in this work is on the behavior of the in-plane metal monolayer excitation at 150 cm^{-1}. This feature is exceptionally sharp and strong—even more

intense than the fundamental excitations of the chalcogenide layers - suggesting that the Cr centers are well-ordered and sit properly on a $\sqrt{3} \times \sqrt{3}$ lattice [Fig. S5, Suppplementary information]. We estimate a phonon lifetime τ_{ph} (from the linewidth) of 4.7 ps, which is unusually long[54,55]. As a reminder, $Cr_{1/3}TaS_2$ is chiral and non-centrosymmetric due to the $x = 1/3$ concentration of *A*-site ions and their hexagonal pattern in the van der Waals gap—just like $Fe_{1/3}TaS_2$[6,29]. This pair of materials allows us to compare the role of *A* site chemistry and size (Cr vs. Fe) while retaining the same TaS_2 chalcogenide layer [Table 1].

In general, pressure will change bond lengths and angles and, at the same time, systematically reduce the van der Waals distance and modify the structural *c*/*a* ratio[30,56–58]. $Cr_{1/3}TaS_2$ is no exception, and the majority of spectral features harden under pressure. Remarkably, even 15 GPa does not significantly distort the 150 cm^{-1} in-plane metal monolayer excitation. There is a small kink in the frequency vs. pressure plot near 2.5 GPa consistent with a change in metal-sulfur interactions, although there is no modification to the hexagonal pattern of the intercalated Cr centers within our sensitivity. The line width of the metal monolayer excitation also broadens with increasing pressure [Fig. 2b], indicating a decrease in the phonon lifetime (from 4.7 ps at ambient conditions to 1.9 ps at 15.5 GPa). The in-plane E_2 symmetry mode of the chalcogenide layer near 342 cm^{-1} also splits into a doublet under compression. The location at which it does so is in good agreement with the aforementioned kink in the frequency vs. pressure plot of the metal monolayer mode. Taken together, the kink and the doublet splitting define a critical pressure of $P_{C,1} = 2.5$ GPa, although the structural distortion is (i) weak and (ii) resides primarily in the chalcogen layers. As a result, it does not strongly impact the overall linear response of the metal monolayer excitation under pressure. Our calculations (detailed below) reveal that the E_2 symmetry mode near 340 cm^{-1} breaks symmetry due to an asymmetric distortion of the hexagons in the chalcogenide layer. Increased pressure thus reduces the space group of $Cr_{1/3}TaS_2$ from $P6_3/22 \rightarrow P321$.

By way of comparison, $Fe_{1/3}TaS_2$ is significantly more flexible with pressure-driven transitions at $P_{C,1} = 3.3$ GPa and $P_{C,2} = 6.0$ GPa, respectively [Fig. 3]. These structural phase transitions involve the chalcogenide layers and the metal monolayers, separating the $P6_3/22$, mixed phase, and high-pressure phases. Analysis of the frequency shifts, splittings, and symmetry restorations provides information about the space group of the high-pressure monoclinic phase which will be discussed elsewhere, although this time, the high-pressure group appears to be *P*3. Key to our discussion below is that the in-plane metal monolayer excitations harden systematically until approximately 3 GPa. Above $P_{C,1}$, the excitation broadens considerably and then splits—a signal of the mixed phase.

At first glance, the difference between these two materials is surprising, so it is important to examine the numbers. The masses on the *A*-site are similar (55.845 vs. 51.996 amu for Fe and Cr, respectively), but the ionic radii are less so (0.780 vs. 0.615 Å) [Table 1]. It appears that, given a van der Waals gap within which to move, the Cr centers are less likely to distort. The van der Waals gap itself is also significantly smaller in $Cr_{1/3}TaS_2$ compared with the Fe analog (2.989 vs. 3.071 Å). Our prior work reveals that pressure-induced structural distortions involving the metal centers in intercalated chalcogenides are blocked when the van der Waals gap becomes too small, or the *A*-site ion becomes too large[44]. Thus, physical and "chemical" pressure yield similar trends in these materials.

In order to better understand the role of metal site substitution in triggering (or blocking) pressure-driven structural transitions, we performed complementary first-principles calculations to reveal specific differences between the Cr and Fe analogs. Overall, we find that the van der Waals gap decreases significantly under compression, whereas layer thickness is actually predicted to increase very slightly with pressure[59]. This explains why the metal monolayer modes are so strongly affected by pressure (more than the layer modes) in these systems. In any case, we find that the metal monolayer mode in $Cr_{1/3}TaS_2$ hardens linearly under pressure, consistent with our experimental findings. It doesn't matter whether our calculations are constrained or not; the properties change smoothly under compression. $Fe_{1/3}TaS_2$ is different. As shown in Fig. 4a, our calculations predict a structural phase transition near 6 GPa due to *c*/*a* effects. Additionally, this dramatic decrease in the van der Waals gap appears to take place with a reduction in the Fe magnetic moment. As shown in Fig. 4b, the moment drops sharply across the transition, consistent

Table 1 | Summary of the characteristic length scales in this set of intercalated chalcogenides[29,32,70]

Material	Crystal structure	*A* site ionic radius (Å)	Layer thickness (Å)	Size of vdW gap (Å)
$Cr_{1/3}TaS_2$	$P6_3/22$, chiral + non-centrosymmetric	0.615	3.145	2.989
$Cr_{1/3}NbS_2$	$P6_3/22$, chiral + non-centrosymmetric	0.615	3.166	2.894
$Fe_{1/3}TaS_2$	$P6_3/22$, chiral + non-centrosymmetric	0.780	3.071	3.071
$Fe_{1/4}TaS_2$	$P6_3/mmc$, centrosymmetric	0.780	3.104	2.973

The valance on the high-spin six-coordinate Cr ion site is 3+ whereas that on the high-spin six-coordinate Fe ion site is 2+[40,71].

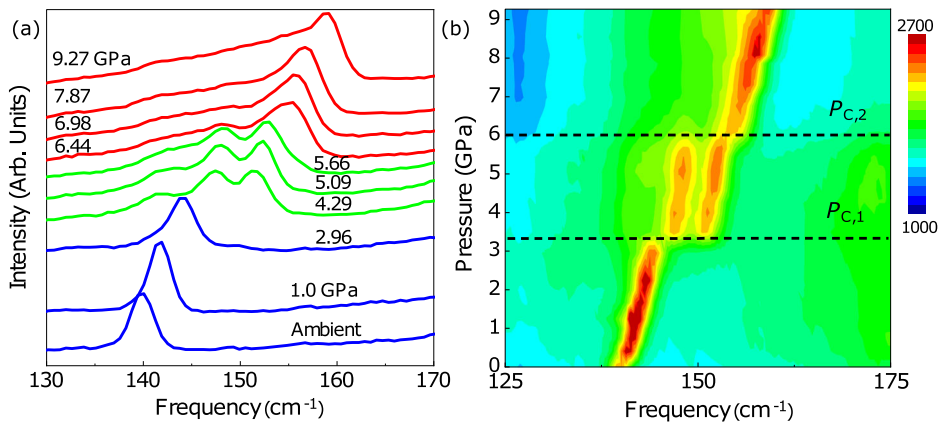

Fig. 3 | Metal monolayer excitation in the Fe analog. a Close-up view of the in-plane metal monolayer mode of $Fe_{1/3}TaS_2$ under compression at 300 K. **b** Contour plot of the same data. The critical pressures are indicated.

with high spin $S = 3/2$ to low spin $S = 1/2$. Since the calculations do not stabilize mixed states, this should be regarded as being in excellent agreement with our experiments.

$Cr_{1/3}TaS_2$ under tensile strain

Given the systematic frequency shift of the in-plane metal monolayer excitation under pressure, we decided to test whether this excitation responds to strain. As shown in Fig. 5, this feature, as well as the many chalcogen layer modes soften under tensile strain. Obviously, the strain applied is small, on the order of 3%, which is sufficient to observe the softening trend but insufficient to induce a phase transition. We find that the superlattice excitation in $Cr_{1/3}TaS_2$ hardens almost linearly under compression and softens linearly under elongation. Going forward, it will be interesting to explore how a softer lattice under strain impacts surface spin wave motion and tunable color properties in this system[32]. Applications in the area of antiferromagnetic spintronics may benefit from structural tunability as well[47–51].

Tunable THz resonators from natural superlattices

One of the most fascinating aspects of the metal monolayer excitations in this family of intercalated chalcogenides is their intensity. In fact, the intensities of these highly collective modes are even stronger than the fundamental *A* and *E* symmetry phonons of the chalcogenide lattices. The line widths are narrow as well. This suggests that metal monolayer excitations might be able to act as tunable teraHertz resonators, perhaps for ultra-fine sensing and flash LiDAR detection[44,52,60–62] or even as tips themselves[53]. Figure S5 in the Supplemental information shows a close-up view of the superlattice excitations in the materials of interest here. The main point is that by judicious choice of the intercalant (including the use of 4- and 5*d* ions), it is possible to position the resonance at different points across the teraHertz range. Small pressures and strains can then be used to refine the position of the collective excitation.

The pressure trends in these materials are interesting and not at all identical. Of the many members of this family of materials that we have studied, $Cr_{1/3}TaS_2$ is likely to be the most useful due to the nearly linear blueshift of the resonance frequency under compression and the relative lack of pressure-driven local lattice distortions. In our hands, the position of the in-plane metal monolayer excitation in $Cr_{1/3}TaS_2$ hardens systematically from 150 to 172 cm^{-1} under 15.5 GPa. This is a frequency shift of nearly 15%. The teraHertz resonance in $Cr_{1/3}NbS_2$ is tunable as well, although slightly less linear, moving from 194 to 209 cm^{-1} over 7.5 GPa—a frequency shift of 10%. As discussed previously, we also tested the ability of the strain to control the position of the in-plane metal monolayer excitation in $Cr_{1/3}TaS_2$ [Fig. 5]. Under modest strain, this excitation softens by 1.5 cm^{-1} (approximately 1%). The total tunability in $Cr_{1/3}TaS_2$ is approximately 16%. We, therefore, see that pressure and strain have the potential to both harden and soften the position of the collective excitation. Whether similar tunability can be anticipated for other materials of this type is still an open question. $Fe_{1/4}TaS_2$ and $Fe_{1/3}TaS_2$, for instance, break symmetry at relatively low pressures. They consequently have a very limited range with a linear response [Fig. 5b and Table S1, Supplementary Information]. By comparison, $Cr_{1/3}TaS_2$ and $Cr_{1/3}NbS_2$ host teraHertz resonances that respond almost linearly under pressure. Taken together, these materials set the stage for the development of a very flexible set of THz resonators.

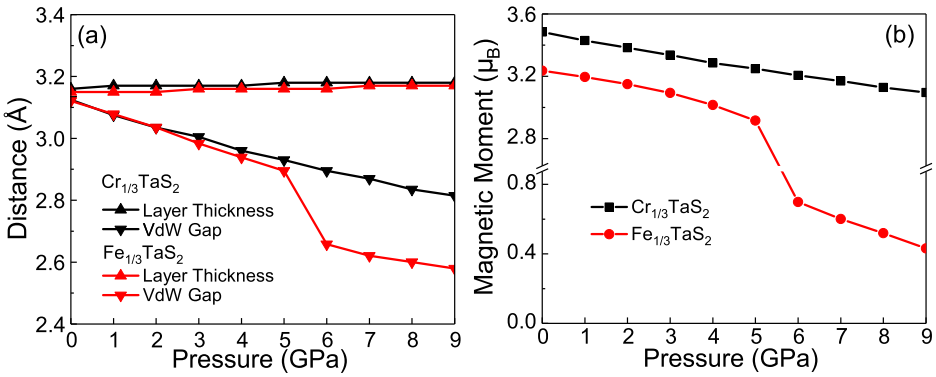

Fig. 4 | First-principles calculations comparing $Cr_{1/3}TaS_2$ and the Fe analog. Density functional theory comparison of **a** layer thickness and van der Waals gap versus pressure for both $Cr_{1/3}TaS_2$ and $Fe_{1/3}TaS_2$ and **b** magnetic moment as a function of pressure for both materials.

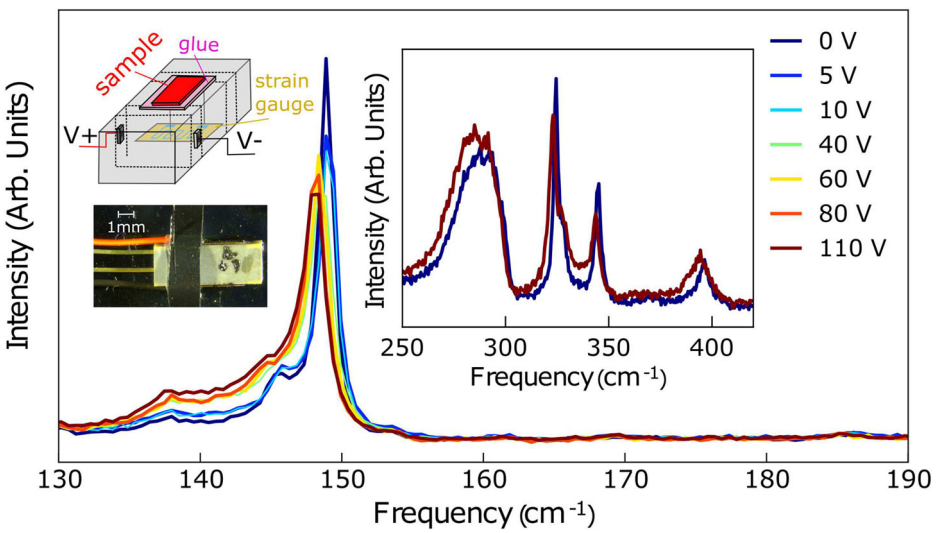

Fig. 5 | Strain measurements. Close-up view of the Raman scattering response of $Cr_{1/3}TaS_2$ as a function of strain at room temperature, focusing on the behavior of the metal monolayer excitation. 100 V corresponds to approximately 3% strain. The insets on the left show a schematic of the piezostack, which operates under voltage control as well as an image of our crystal on the piezostack. The right-hand inset shows that the chalcogen layer phonons soften under tensile strain.

Discussion

Thus far, we have combined Raman scattering spectroscopy with diamond anvil cell techniques and complementary first-principles calculations to explore the low-frequency excitations of a series of natural superlattices in the form of intercalated chalcogenides. Each material hosts in- and out-of-plane excitations of the intercalated metal monolayer that resonates in the teraHertz range. The exact resonance frequency of these collective excitations depends upon the chemical identity and loading of the intercalent. In principle, the resonance frequency can be tuned across much of the useful teraHertz range in this manner. Pressure and strain are useful external stimuli in certain cases as well. We find that while the metal monolayer excitations in Fe_xTaS_2 ($x = 1/4, 1/3$) distort significantly under compression, the same excitation in related systems, including $Cr_{1/3}TaS_2$ and $Cr_{1/3}NbS_2$ shifts almost linearly under pressure and strain. We discuss these trends in terms of the chalcogen layer thickness and size of the van der Waals gap compared to the size of the *A* site ion. These structure–property relations, along with the linear responsivity of the teraHertz resonance under pressure and strain, pave the way for various spintronics and photonics applications.

Methods

Crystal growth and loading of the diamond anvil cell

High-quality single crystals of several different intercalated transition metal dichalcogenides were grown via flux techniques as described previously[29]. The concentration of Cr was determined using a combination of energy-dispersive X-ray spectroscopy (EDX) and the saturated magnetic moment obtained from measurements of the magnetic moment as a function of the magnetic field (*M*–*H*) at 2 K. We selected $Cr_{1/3}TaS_2$, $Cr_{1/3}NbS_2$, $Fe_{1/3}TaS_2$, and $Fe_{1/4}TaS_2$ in order to explore structure-property relations in this family of materials. That said, the majority of work focuses on $Cr_{1/3}TaS_2$ and $Cr_{1/3}NbS_2$, with only brief comparisons to the Fe analogs. Small, well-shaped pieces of each crystal were selected and loaded into suitably chosen diamond anvil cells with either KBr as the pressure medium to ensure quasi-hydrostatic pressure conditions [Fig. S1, Supplemental information]. An annealed ruby ball was included to determine pressure via fluorescence [Fig. S2, Supplemental information][63,64]. Two different symmetric diamond anvil cells were used in this work. Both employed synthetic high temperature-high pressure type II as low fluorescence diamonds with either 500 or 600 μm culets. These measurements employed 50 μm thick pre-indented stainless steel gaskets with 200 μm diameter holes.

Raman scattering under pressure

We performed Raman scattering measurements (10–600 cm^{-1}) using a 532 nm (green) laser with 3.5 mW power, a triple monochromator, and a liquid nitrogen-cooled CCD detector. Scans were between 30 and 60 s, averaged 5 or 10 times depending on the need. The pressure was increased between 0 and approximately 11 GPa at room temperature. We monitored the shape of the ruby fluorescence spectrum before each measurement to ensure that the sample remained in a quasi-hydrostatic environment. We compare the Raman scattering spectra of pristine and pressure-cycled $Cr_{1/3}TaS_2$ in Figs. S3 and S4, Supplemental information.

Raman scattering under strain

To complement high-pressure work in the diamond anvil cell, we also performed Raman scattering spectroscopy under strain on selected samples. Piezostacks operating under voltage control provide access to both compressive and elongational strain effects [inset, Fig. 4]. It is very important to use thin crystals (less than 10 μm) so that strain remains uniform across the sample. Strain is linearly proportional to the voltage. We calibrate the relationship between applied voltage and strain using distance markers as described elsewhere[32]. In our case, 100 V is equivalent to approximately 3% tensile strain.

First-principles calculations

To understand the change in the structural and magnetic properties, density functional calculations were performed using QuantumATK within a spin-polarized generalized gradient approximation (SGGA), a Perdew, Burke, and Ernzerhof (PBE) exchange-correlation, and a PseudoDojo pseudopotential[65–68]. The calculations were run with a Grimme DFT-D3 van der Waals correction[69]. Structures were geometry optimized to a maximum force of 0.01 Å/eV and applied constrained and unconstrained isotropic pressure from 0 to 9 GPa. The calculations used a k-point sampling of $6 \times 6 \times 3$ with a tolerance of 10^{-5} Hartrees.

Data availability

Data is provided within the paper or supplementary information files.

Received: 24 October 2024; Accepted: 22 January 2025;
Published online: 03 March 2025

References

1. Gamble, F. R. et al. Intercalation complexes of Lewis bases and layered sulfides: a large class of new superconductors. *Science* **174**, 493–497 (1971).
2. Yu, Y. et al. Enhancing multifunctionalities of transition-metal dichalcogenide monolayers via cation intercalation. *ACS Nano* **11**, 9390 (2017).
3. Wang, Z. et al. Intercalated phases of transition metal dichalcogenides. *Smart Mat.* **1**, e1013 (2020).
4. Rajapakse, M. et al. Intercalation as a versatile tool for fabrication, property tuning, and phase transitions in 2D materials. *npj 2D Mater. Appl.* **5**, 30 (2021).
5. Tezze, D. et al. Tuning the magnetic properties of $NiPS_3$ through organic-ion intercalation. *Nanoscale* **14**, 1165–1173 (2022).
6. He, Q. et al. Direct synthesis of controllable ultrathin heteroatoms-intercalated 2D layered materials. *Nat. Commun.* **15**, 6320 (2024).
7. Snow, C. S. et al. Quantum melting of the charge-density-wave in 1*T*-$TiSe_2$. *Phys. Rev. Lett.* **91**, 136402 (2003).
8. Morosan, E. et al. Superconductivity in Cu_xTiSe_2. *Nat. Phys.* **2**, 544–550 (2006).
9. Barath, H. et al. Quantum and classical mode softening near the charge density wave—superconductor transition in Cu_xTiSe_2. *Phys. Rev. Lett.* **100**, 106402 (2008).
10. Kusmartseva, A. F. et al. Pressure induced superconductivity in pristine 1*T*-$TiSe_2$. *Phys. Rev. Lett.* **103**, 236401 (2009).
11. Yan, S. et al. Influence of domain walls in the incommensurate charge density wave state of Cu intercalated 1T-$TiSe_2$. *Phys. Rev. Lett.* **118**, 106405 (2017).
12. Togawa, Y. et al. Anomalous temperature behavior of the chiral spin helix in $CrNb_3S_6$ thin lamellae. *Phys. Rev. Lett.* **122**, 017204 (2019).
13. Aoki, R. et al. Anomalous nonreciprocal electrical transport on chiral magnetic order. *Phys. Rev. Lett.* **122**, 057206 (2019).
14. Tang, S. et al. Tuning magnetic soliton phase via dimensional confinement in exfoliated 2D $Cr_{1/3}NbS_2$ thin flakes. *Nano Lett.* **18**, 4023–4028 (2018).
15. Clements, E. M. et al. Magnetic field dependence of nonlinear magnetic response and tricritical point in the monoaxial chiral helimagnet $Cr_{1/3}NbS_2$. *Phys. Rev. B* **97**, 214438 (2018).
16. Wang, L. et al. Controlling the topological sector of magnetic solitons in exfoliated $Cr_{1/3}NbS_2$ crystals. *Phys. Rev. Lett.* **118**, 257203 (2017).
17. Ghimire, N. J. et al. Magnetic phase transition in single crystals of the chiral helimagnet $Cr_{1/3}NbS_2$. *Phys. Rev. B* **87**, 104403 (2013).
18. Togawa, Y. et al. Chiral magnetic soliton lattice on a chiral helimagnet. *Phys. Rev. Lett.* **108**, 107202 (2012).
19. Tenasini, G. et al. Giant anomalous Hall effect in quasi-two-dimensional layered antiferromagnet $Co_{1/3}NbS_2$. *Phys. Rev. Res.* **2**, 023051 (2000).
20. Sirica, N. et al. The nature of ferromagnetism in the chiral helimagnet $Cr_{1/3}NbS_2$. *Commun. Phys.* **3**, 65 (2020).
21. Liu, H. et al. Elastically induced magnetization at ultrafast time scales in a chiral helimagnet. *Phys. Rev. B* **106**, 035103 (2022).

22. Karna, S. K. et al. Annihilation and control of chiral domain walls with magnetic field. *Nano Lett.* **21**, 1205–1212 (2021).
23. Park, P. et al. Tetrahedral triple-Q magnetic ordering and large spontaneous Hall conductivity in the metallic triangular antiferromagnet $Co_{1/3}TaS_2$. *Nat. Commun.* **14**, 8346 (2023).
24. Park, P. et al. Composition dependence of bulk properties in the Co-intercalated transition metal dichalcogenide $Co_{1/3}TaS_2$. *Phys. Rev. B* **109**, L060403 (2024).
25. Radovsky, G. et al. Nanotubes from chalcogenide misfit compounds: Sn-S and Nb-Pb-S. *Acc. Chem. Res.* **47**, 406–416 (2014).
26. Sreedhara, M. B. et al. Nanotubes from the misfit layered compound $(SmS)_{1.19}TaS_2$: atomic structure, charge transfer, and electrical properties. *Chem. Mater.* **34**, 1838–1853 (2022).
27. Nawaz Tahir, M. et al. Synthesis and functionalization of chalcogenide nanotubes. *Phys. Stat. Sol. (b)* **247**, 2338–2363 (2010).
28. Morosan, E. et al. Sharp switching of the magnetization in $Fe_{1/4}TaS_2$. *Phys. Rev. B* **75**, 104401 (2007).
29. Horibe, Y. et al. Color theorems, chiral domain topology, and magnetic properties of Fe_xTaS_2. *J. Am. Chem. Soc.* **136**, 8368–8373 (2014).
30. Mito, M. et al. Investigation of structural changes in chiral magnet $Cr_{1/3}NbS_2$ under application of pressure. *J. Appl. Phys.* **117**, 183904 (2015).
31. Liu, Y. et al. Electrical and thermal transport in van der Waals magnets 2H-$M$$TaS_2$ (M = Mn, Co). *Phys. Rev. Res.* **4**, 013048 (2022).
32. Du, K. et al. Strain-control of cycloidal spin order in a metallic van der Waals magnet. *Adv. Mater.* **35**, 2303750 (2023).
33. Xie, L. S. et al. Structure and magnetism of iron- and chromium-intercalated niobium and tantalum disulfides. *J. Am. Chem. Soc.* **144**, 9525–9542 (2022).
34. Husremovic, S. et al. Hard ferromagnetism down to the thinnest limit of iron-intercalated tantalum disulfide. *J. Am. Chem. Soc.* **144**, 12167–12176 (2022).
35. An, Y. et al. Bulk properties of the chiral metallic triangular antiferromagnets $Ni_{1/3}NbS_2$ and $Ni_{1/3}TaS_2$. *Phys. Rev. B* **108**, 054418 (2023).
36. Du, K. et al. Topological spin-structure couplings in layered chiralmagnet $Cr_{1/3}TaS_2$2: the discovery of spiral magnetic superstructure. *Proc. Natl Acad. Sci. USA* **118**, e2023337118 (2021).
37. Hu, W. Z. et al. Optical study of the charge-density-wave mechanism in 2H-TaS_2 and Na_xTaS_2. *Phys. Rev. B* **76**, 045103 (2007).
38. Mankovsky, S. et al. Electronic, magnetic, and transport properties of Fe-intercalated 2H-TaS_2 studied by means of the KKR-CPA method. *Phys. Rev. B* **92**, 144413 (2015).
39. Fan, S. et al. Electronic chirality in the metallic ferromagnet $Fe_{1/3}TaS_2$. *Phys. Rev. B* **96**, 205119 (2017).
40. Xie, L. S. et al. Comparative electronic structures of the chiral helimagnets $Cr_{1/3}NbS_2$ and $Cr_{1/3}TaS_2$. *Chem. Mater.* **35**, 7239–7251 (2023).
41. Li, L. J. et al. Fe-doping-induced superconductivity in the charge-density-wave system 1T-TaS_2. *Eur. Phys. Lett.* **97**, 67005 (2012).
42. Wu, S. et al. Discovery of charge order in the transition metal dichalcogenide Fe_xNbS_2. *Phys. Rev. Lett.* **131**, 186701 (2023).
43. Takagi, H. et al. Spontaneous topological Hall effect induced by non-coplanar antiferromagnetic order in intercalated van der Waals materials. *Nat. Phys.* **19**, 961–968 (2023).
44. Fan, S. et al. Excitations of intercalated metal monolayers in transition metal dichalcogenides. *Nano Lett.* **21**, 99–106 (2021).
45. Erodici, M. P. et al. Bridging structure, magnetism, and disorder in iron-intercalated niobium diselenide, Fe_xNbSe_2, below $x = 0.25$. *J. Phys. Chem. C* **127**, 9787–9795 (2023).
46. Grasset, R. et al. Pressure-induced collapse of the charge density wave and Higgs mode visibility in 2H-TaS_2. *Phys. Rev. Lett.* **122**, 127001 (2019).
47. Nair, N. L. et al. Electrical switching in a magnetically intercalated transition metal dichalcogenide. *Nat. Mater.* **19**, 153–157 (2020).
48. Little, A. et al. Three-state nematicity in the triangular lattice antiferromagnet $Fe_{1/3}NbS_2$. *Nat. Mater.* **19**, 1062–1067 (2020).
49. Yang, S. H. Spintronics on chiral objects. *Appl. Phys. Lett.* **116**, 120502 (2020).
50. Amin, O. J. et al. Electrical control of antiferromagnets for the next generation of computing technology. *Appl. Phys. Lett.* **117**, 010501 (2020).
51. Mi, M. et al. Two-dimensional magnetic materials for spintronic devices. *Mater. Today Nano* **24**, 100408 (2023).
52. Ryzhii, V. et al. Detection of terahertz radiation using topological graphene micro- nanoribbon structures with transverse plasmonic resonant cavities. *J. Appl. Phys.* **136**, 194502 (2024).
53. Pistore, V. et al. Near-field probes for sensitive detectorless near-field nanoscopy in the 2.0-4.6 THz range. *Appl. Phys. Lett.* **124**, 221105 (2024).
54. Sun, Q.-C. et al. Observation of a Burstein-Moss shift in Re-doped MoS_2 nanoparticles. *ACS Nano* **7**, 3506–3511 (2013).
55. Gu, Y. et al. Phonon mixing in the charge density wave state of ScV_6Sn_6. *npj Quantum Mater.* **8**, 58 (2023).
56. Grochala, W. et al. The chemical imagination at work in very tight places. *Angew. Chem. Int. Ed.* **46**, 3620–3642 (2007).
57. Pei, S. et al. High pressure studies of 2D materials and heterostructures: a review. *Mater. Des.* **213**, 110363 (2022).
58. Matsuoka, T. et al. MPX_3 van der Waals magnets under pressure (M = Mn, Ni, V, Fe, Co, Cd; X = S, Se). *Front. Mater.* **11**, 1362744 (2024).
59. The intercalate layer acts as a cushion for the TaS_2 layer. Since we are applying isotropic pressure to the system, the 2D layer of TaS_2 is mainly compressed in the *ab* plane and relieves some of the strain along the *c* axis, slightly increasing the layer thickness. This trend is obviously very slight.
60. Choi, C. Q. Three practical uses for topological photonics. *IEEE Spectr.* **57**, 9–10 (2020).
61. Yang, Y. et al. Terahertz topological photonics for on-chip communication. *Nat. Photonics* **14**, 446–451 (2020).
62. Liu, Y. et al. Flexible broadband teraHertz modulation based on strain-sensitive MXene material. *Front. Phys.* **9**, 670972 (2021).
63. Mao, H. K. et al. Specific volume measurements of Cu, Mo, Pd, and Ag and calibration of the ruby R_1 fluorescence pressure gauge from 0.06 to 1 Mbar. *J. Appl. Phys.* **49**, 3276–3283 (1976).
64. Mao, H. K. et al. Calibration of the ruby pressure gauge to 800 kbar under quasi-hydrostatic conditions. *J. Geophys. Res.* **91**, 4673–4676 (1986).
65. QuantumATK version R-2020.09.
66. Smidstrup, S. et al. QuantumATK: An integrated platform of electronic and atomic-scale modelling tools. *J. Phys: Condens. Matter* **32**, 015901 (2020).
67. Perdew, J. P. et al. Generalized gradient approximation made simple. *Phys. Rev. Lett.* **778**, 3865 (1996).
68. Van Setten, M. J. et al. The PseudoDojo: training and grading a 85 element optimized norm-conserving pseudopotential table. *Comput. Phys. Commun.* **226**, 39 (2018).
69. Caldeweyher, E. et al. Extension of the D3 dispersion coefficient model. *J. Chem. Phys.* **147**, 034112 (2017).
70. Miyadai, T. et al. Magnetic properties of $Cr_{1/3}NbS_2$. *JUPSAU* **52**, 1394–1401 (1983).
71. Ko, K.-T. et al. RKKY ferromagnetism with Ising-like spin states in intercalated $Fe_{1/4}TaS2_2$. *Phys. Rev. Lett.* **107**, 247201 (2011).

Acknowledgements

J.L.M. thanks Physical Behavior of Materials, Basic Energy Sciences, U.S. Department of Energy (Contract number DESC0023144) for support of this work. S.W.C. was funded by the W. M. Keck foundation grant to the Keck Center for Quantum Magnetism at Rutgers University. D.M. acknowledges funding from the Gordon and Betty Moore Foundation's EPiQS Initiative, Grant GBMF9069. J.Y. acknowledges support by DOE under Grant No. DOE: DE-SC0021188. J.T.H. acknowledges support from the Institute for Materials Science at Los Alamos National Laboratory. This work used resources of the National Synchrotron Light Source II; a U.S. Department of

Energy (DOE) Office of Science User Facility operated for the DOE Office of Science by Brookhaven National Laboratory under Contract No. DESC0012704. Use of the 22-IR-1 beamline is supported by the National Science Foundation Division of Earth Sciences (EAR) SEES: Synchrotron Earth and Environmental Science (EAR-2223273) and Chicago/DOE Alliance Center (CDAC) DE-NA-0004153. We thank B. Donahoe and S. Fan for useful conversations.

Author contributions

J.L.M. designed the study. P.Y., J.Y., S.W.C., and D.M. grew the crystals. J.L.M. and Z.L. performed the high-pressure spectroscopic measurements. Y.G. carried out the strain studies. J.T.H. performed complementary first-principles calculations. J.L.M. analyzed the spectral data. J.L.M., Y.G., and J.T.H. designed the figures. J.L.M. drafted the paper. All authors read and commented on the text.

Competing interests

Authors J.L.M., Y.G., J.T.H., K.D., P.Y., J.Y., D.G.M., and Z.L. declare no competing interests. Author S.W.C. serves as an editor of this journal and had no role in the peer-review or decision to publish this paper. Author S.W.C. declares no competing interests.

Additional information

Supplementary information The online version contains supplementary material available at https://doi.org/10.1038/s41535-025-00734-x.

Correspondence and requests for materials should be addressed to J. L. Musfeldt.